Ocean Engineering 252 (2022) 111242

Contents lists available at ScienceDirect

Ocean Engineering

journal homepage: www.elsevier.com/locate/oceaneng

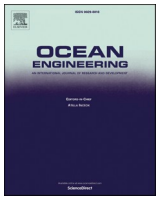

Study on the cavity dynamics of water entry for horizontal objects with different geometrical shapes

Yan Du [a,b], Zhiying Wang [a,*], Yiwei Wang [a,b,c], Jingzhu Wang [a], Rundi Qiu [a,b,c], Chenguang Huang [d]

[a] Key Laboratory for Mechanics in Fluid Solid Coupling Systems, Institute of Mechanics, Chinese Academy of Sciences, Beijing, 100190, China
[b] School of Engineering Science, University of Chinese Academy of Sciences, Beijing, 100049, China
[c] School of Future Technology, University of Chinese Academy of Sciences, Beijing, 100049, China
[d] Hefei Institutes of Physical Science, Chinese Academy of Sciences, Hefei, 230031, China

ARTICLE INFO

Keywords:
Water entry
Cavity dynamics
Pinch-off depth
Vortex evolution

ABSTRACT

The influence of geometrical shapes on cavity evolution, flow fields and vortex structures evolution during water entry processes are investigated by experimental and numerical methods in this paper. The cavity evolution for water entry of four horizontal objects with different geometrical shapes are captured by high-speed photography. The experimental results indicate that although the geometrical shape has influence on cavity shape and size, the pinch-off depths are very close for the open cavity cases. In the numerical study, a compressible two-phase flow solver combing with large eddy simulation (LES) and dynamic overset mesh based on OpenFOAM® platform is adopted to observe the cavity dynamics, flow fields and vortex structures information. Numerical results reveal that the cavity produced by the object with trapezoid section expand at a relatively higher speed in the radial direction to form a larger cavity due to the more kinetic energy transference to the fluid. The vorticity evolution shows that for the object with circle section, the vortex structures alternately shed at the cavity tail shortly after the cavity separates from the free surface. However, for the object with trapezoid section, the cavity is squashed distorted due to the hydrostatic pressure without alternating vortex shedding.

1. Introduction

Water entry is a common phenomenon which refers to the process when structures impact and travel through the free surface into water. Many researches have been conducted for on certain applications, such as seaplane landing (von Karman, 1929), missiles entry (May, 1953, 1975), Hull slamming (Zhao and Faltinsen, 1993; Abrate, 2013), coastal protection facilities (Sruthi and Sriram, 2017) and crashworthiness of aerospace structures (Seddon and Moatamedi, 2006).

Geometrical shape of entry structure will absolutely affect the water entry. There are researches focusing on effect of nose shapes for slender projectiles on cavity or splash morphological evolution, forces and trajectory. Bodily et al. (2014) compared the forces, velocities, and trajectories of slender projectiles with cone, ogive and flat nose shape using an embedded inertial measurement unit (IMU). The largest lateral displacement is achieved by cone nose and the largest impulsive force is experienced by the flat nose. Shi et al. (2019) studied the effect of nose shapes on pinch-off based, the results show that the blunt nose shapes can speed up the surface seal and then quicken the pinch-off. Yan et al. (2019) investigate the influence of nose shape of projectile on the jet flow and the cavity diameter. Shi et al. (2020) studied the asymmetry of nose on trajectory experimentally and established a theoretical model of projectile motion. The effect of nose shape on trajectory stability has also been illustrated numerically (Chen, 2019; Song et al., 2020; Wang et al., 2021).

When deep seal occurs for slender bodies, pinch-off can occur on the body of the projectile (Bodily et al., 2014), thus altering the jet formation. To further explore the cavity morphological evolution or dynamics of water entry, some non-slender shapes such as sphere (May and Woodhull, 1950; Duez et al., 2007; Mansoor et al., 2014; Li et al., 2020; Sun et al., 2019, 2021), cylinder (Duclaux et al., 2007; Gekle, 2008), wedge (Vincent et al., 2018), and disk (Glasheen 1996; Bergmann et al., 2009) are picked as the research object. Duclaux et al. (2007) found an approximate analytical solution which describes the cavity evolution when inertia dominates viscous and capillary effects, and conducted experiments of sphere and cylinder for validation, the characteristics of

* Corresponding author.
E-mail address: wangzhiying@imech.ac.cn (Z. Wang).

https://doi.org/10.1016/j.oceaneng.2022.111242
Received 26 December 2021; Received in revised form 21 March 2022; Accepted 30 March 2022
Available online 9 April 2022
0029-8018/© 2022 Elsevier Ltd. All rights reserved.

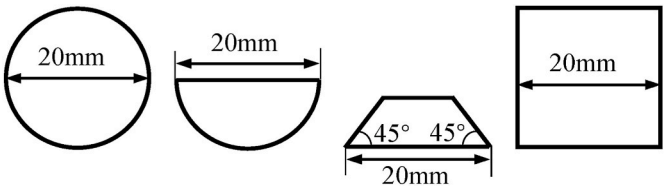

Fig. 1. The schematic of the sections' shapes and sizes of horizontal water entry objects.

the experimental cavities agree well with those expected from the theory. Duez et al. (2007) determined the threshold velocity for air entrainment (cavity formation) as a function of static contact angle for sphere. Aristoff and Bush (2009) established a mathematical model describing the cavity evolution based on the solution of the Rayleigh–Besant problem to predict the pinch off time and depth. The water entry process of sphere has been systematically studied, and there have also been some studies that concerned other geometry structures. Aristoff et al. (2010) investigated vertical impact of low-density spheres and characterized the sphere dynamics and the influence of its deceleration on the shape of the resulting air cavity on a water surface. Korkmaz and Guzel (2017) studied the water entry process of cylinder under hydrophobic effects and found that hydrophobicity causes larger pileups with faster jet flows indicating more kinetic energy transference to the fluid. Wei and Hu (2014) investigated the three-dimensional effect of water entry of horizontal cylinder and concluded that the speed of the jetting formed by a horizontal cylinder is about 1.5 times of that by a sphere. Vincent et al. (2018) experimentally characterized the shapes of the cavity and splash created by the wedge and proposed a one-dimensional model of the splash that take gravity, surface tension and aerodynamics forces into account. Glasheen and Mcmahon (1996) measured the force during the water entry process of disk and found that

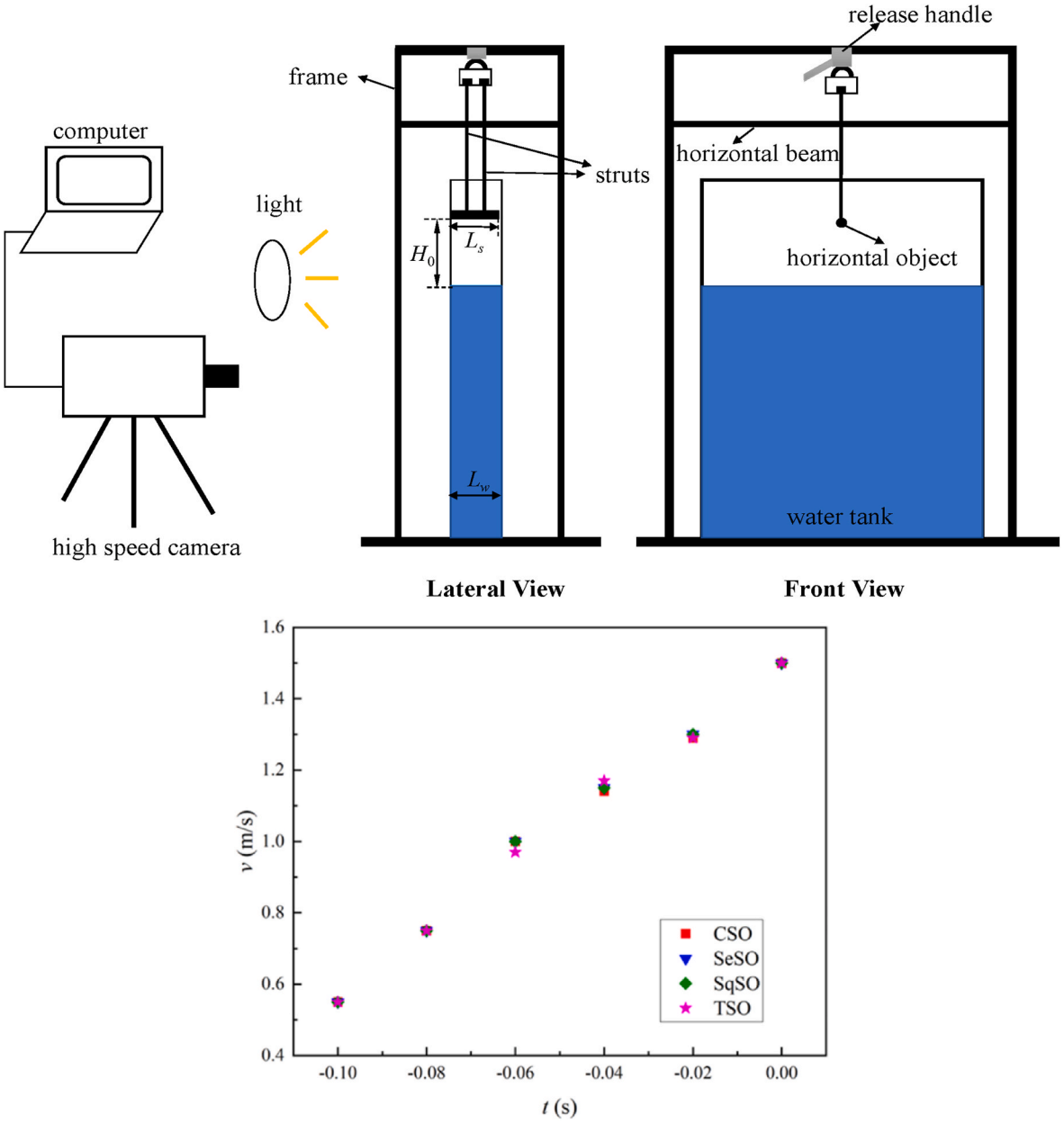

Fig. 2. (a). The schematic of the experimental apparatus. The object is released by pulling the handle. Fig. 2(b). The velocity before water entry for different objects. $t = 0$ is the moment when the object touches the free surface and the negative time indicates the time before water entry. The positive direction of y is down along the free surface.

Table 1
The test conditions in the experiment.

	H_0 (cm)	U_0 (m/s)
Case1	9	1.07 m/s
Case2	15	1.50 m/s
Case3	24	1.92 m/s

the force impulse is caused by acceleration of the virtual mass of fluid. Bergmann et al. (2009) found the scaling of pinch-off depth and total depth roughly as $\propto$ Fr1/2 for disk entry. Enriquez et al. (2012) observed more complex pinch-off modes of disk water entry by creating non-axisymmetric air cavities characterized by azimuthal harmonic disturbances.

Non-slender entry structures with different geometric shapes have been studied dividedly, but the effects of geometric shape lack of comparison systematically. Relatively speaking, the water entry of non-slender entry structures will be more suitable for investigating the cavity evolution and dynamics since the cavity attached to a non-slender structure won't be affected by the entry structure as it is attached to a slender body. So, it's necessary to explore and compare water entry process of non-slender structure with different geometrical shapes.

In this paper, the cavities evolution for water entry of four objects with different geometrical shape were obtained and compared based on constraint launching system and high-speed photography. Besides, numerical simulations for two typical structures, circle section object (CSO) and trapezoid section object (TSO), were conducted within the OpenFOAM® framework to analyze the differences in flow fields and vortex structures evolutions for the shallow and deep seal patterns caused by circle and trapezoid sections respectively.

This paper is organized in the following manner. The experiment setup and physical parameters is described in Section 2. Section 3 illustrates the governing equations and numerical methods. Section 4.1 analyzes and compares the cavities and splashes evolutions of five horizontal objects according to the experimental results. The validation for numerical results and the comparation of flow fields for CSO and TSO are given in Section 4.2 Section 4.3 discusses the differences of vortex structures evolutions caused by various closure patterns.

2. Experimental setup

Four test objects with different section shapes that are circle section, semicircle section, square section and trapezoid section, as shown in Fig. 1, are investigated in this study. The characteristic length of each objects L_0 ($L_0 = 2R_0$) is 20 mm and the span length L_s of the objects is designed to be 150 mm.

A schematic of the experimental setup is shown in Fig. 2(a). The object is guided by two long rods to achieve vertical water entry. The water tank has a size of 800mm × 600mm × 152 mm whose span length L_w is slightly longer than the L_s. Therefore, the three-dimensional effect can be avoided (Wei, 2014) and quasi two-dimensional cavity is obtained. We release the objects at three initial heights H_0, the H_0 and measured entry velocity U_0 is shown in Table 1 and the velocity before water entry for different objects in Case2 is measured as shown in Fig. 2 (b). It can be seen that the experimental apparatus won't bring remarkable difference for entry velocity.

The high-speed camera Phantom V1612 matched with 24–70 mm focal length's lens is used to capture the process of the water entry. The frame is set to be 4000 fps with a resolution of 1280 × 800 pixels.

3. Numerical method

3.1. Governing equations

3.1.1. Fluid equations

We adopt a compressible homogeneous two-phase model in this paper, the mass conservation equations is as follows:

$$\frac{\partial \rho}{\partial t} + \nabla \cdot (\rho \boldsymbol{u}) = 0 \tag{1}$$

where the symbol ρ is the mixture density defined as $\rho = \rho_l \alpha_l + \rho_a \alpha_a$, the subscripts a and l represent air and water respectively, $\boldsymbol{u}$ denotes the velocity field shared by all the phases. The constraint $\alpha_l + \alpha_a = 1$ should be satisfied. The momentum equation for the mixture is as follows:

$$\frac{\partial \rho u}{\partial t} + \nabla \cdot (\rho \boldsymbol{u}\boldsymbol{u}) = -\nabla p + \nabla \cdot \left[\mu \left(\nabla \boldsymbol{u} + (\nabla \boldsymbol{u})^T - \frac{2}{3} (\nabla \cdot \boldsymbol{u}) \boldsymbol{I} \right) \right] + \sigma \kappa \nabla \alpha_l \tag{2}$$

while μ, σ, κ respectively denotes dynamic viscosity, surface tension coefficient and curvature. The third term on the right side represents the effect of surface tension force, which is active only within vicinity of the interfaces of liquid water and air, cavity boundary and free surface. p is the pressure caused by fluid motion which excludes hydrostatic pressure under the effect of gravity.

The energy equation for the mixture is:

$$\frac{\partial}{\partial t} [\rho (K + e)] + \nabla \cdot [\rho \boldsymbol{u} (K + e)] = \nabla \cdot (\boldsymbol{u} \cdot \boldsymbol{\tau}) - \nabla \cdot \boldsymbol{q} - \nabla \cdot (\boldsymbol{u} p) \tag{3}$$

where K, e, q is kinetic energy, internal energy and heat flux density respectively. They can be defined as: $K = 0.5|\mathrm{u}|^2$, $e = C_v T$, $q = -\alpha^{th} C_v \nabla T$. C_v represents the special heat capacity, and α^{th} is the thermal diffusivity. Thus, the equation for temperature T can simplified as:

$$\frac{\partial}{\partial t} (\rho C_v T) + \nabla \cdot (\rho C_v T \boldsymbol{u}) - \nabla \cdot \left(\alpha^{th} C_v \nabla T \right) = -\nabla \cdot (p \boldsymbol{u}) - \frac{\partial}{\partial t} (\rho K) - \nabla \cdot (\rho K \boldsymbol{u}) \tag{4}$$

3.1.2. Rigid body motion equations

For a single moving body without rotation, the linear acceleration $\boldsymbol{a}$ can be formulated by:

$$\boldsymbol{a} = \boldsymbol{F}/m \tag{5}$$

Where $\boldsymbol{F}$ denotes the external force, m is the mass of the rigid body. $\boldsymbol{F}$ can be calculated by physical quantity of flow fields:

$$\boldsymbol{F} = \iint_S (p\boldsymbol{I} + \tau) \cdot d\boldsymbol{S} + m\boldsymbol{g} \tag{6}$$

where $\boldsymbol{I}$ is the identity matrix, $\boldsymbol{\tau}$ is the viscous stress, $\boldsymbol{S}$ denotes the surface of the boundary patch for the moving body. The velocity $\boldsymbol{u}$ and displacement $\boldsymbol{x}$ can be obtained by:

$$\boldsymbol{u}_n^{k+1} = \boldsymbol{u}_o + \triangle t \left(\gamma \boldsymbol{a}_n^k + (1 - \gamma) \boldsymbol{a}_o \right) \tag{7}$$

$$\boldsymbol{x}_n^{k+1} = \boldsymbol{x}_o + \boldsymbol{u}_o \triangle t + \beta (\triangle t)^2 \boldsymbol{a}_n^k + (0.5 - \beta)(\triangle t)^2 \boldsymbol{a}_o \tag{8}$$

The subscript "o" and "n" represent old and new respectively, and the superscript "k" or "k+1" means the k or k+1 sub-iteration. γ and β are two parameters in Newmark solver type. We adopt $\gamma = 0.5$ and $\beta = 0.25$ in this paper.

3.2. Turbulence modeling

The Favre-filtering operation is applied to perform large eddy simulation (LES). The large scales are resolved directly from the instantaneous Navier–Stokes equation while the small scales are represented by subgrid scale (SGS) models. The momentum and temperature equations are filtered as:

$$\frac{\partial \widetilde{\rho \mathrm{u}}}{\partial t} + \nabla \cdot (\widetilde{\rho \mathrm{u}\mathrm{u}}) = -\nabla \overline{p} + \nabla \cdot \overline{\tau} + \sigma \kappa \nabla \overline{\alpha}_1 + \nabla \cdot \tau_{SGS} \tag{9}$$

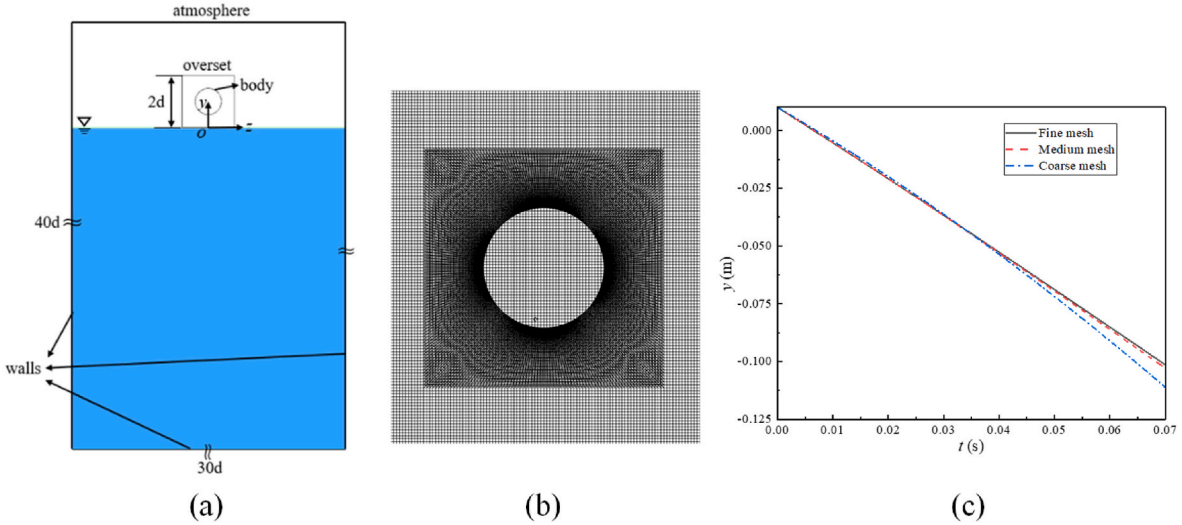

Fig. 3. (a) The domain and boundary conditions in the simulation, d denotes the diameter of the circle, $y = 0$ is set at the initial free surface. (b) the computational mesh near the water entry object and (c) Time histories of the y-coordinate of the center of the cylinder with three different grid levels.

$$\frac{\partial}{\partial t}\left(\overline{\rho}C_v\widetilde{T}\right)+\nabla\cdot\left(\overline{\rho}C_v\widetilde{T}\widetilde{\mathrm{u}}\right)+\frac{\partial}{\partial t}\left(\overline{\rho}\frac{\widetilde{\mathrm{u}}\cdot\widetilde{\mathrm{u}}}{2}\right)+\nabla\cdot\left(\overline{\rho}\frac{\widetilde{\mathrm{u}}\cdot\widetilde{\mathrm{u}}}{2}\widetilde{\mathrm{u}}\right)=\nabla\cdot\left(\alpha^{th}C_v\nabla\overline{T}\right)-\nabla\cdot\left(\overline{p}\widetilde{\mathrm{u}}\right)+\nabla\cdot\mathrm{Q}_{SGS} \tag{10}$$

where the tilde quantities are Favre averaged ones. $\boldsymbol{\tau_{SGS}}$, $\boldsymbol{Q_{SGS}}$ are SGS stress and SGS heat flux generated from nonlinear in governing equations that are need to be modelled. The one-equation eddy viscosity model is adopted in which the SGS eddy-viscosity ν_{SGS} and dissipation are defined as

$$\nu_{SGS}=C_k\frac{k_{SGS}^{1/2}}{\Delta} \tag{11}$$

$$\varepsilon=C_\varepsilon\frac{k_{SGS}^{3/2}}{\Delta} \tag{12}$$

where Δ denotes filter width that is chosen as cube-root of the cell volume in this study, coefficients are given as $C_k = 0.094$, $C_\varepsilon = 1.048$. The transport equation of SGS kinetic energy k_{SGS} is

$$\frac{\partial(\overline{\rho}k_{SGS})}{\partial t}+\nabla\cdot(\overline{\rho}\widetilde{\mathrm{u}}k_{SGS})-\nabla\cdot[\overline{\rho}(\nu+\nu_{SGS})\nabla k_{SGS}]=-\overline{\rho}\tau_{SGS}:\overline{\mathbf{D}}-\overline{\rho}\varepsilon \tag{13}$$

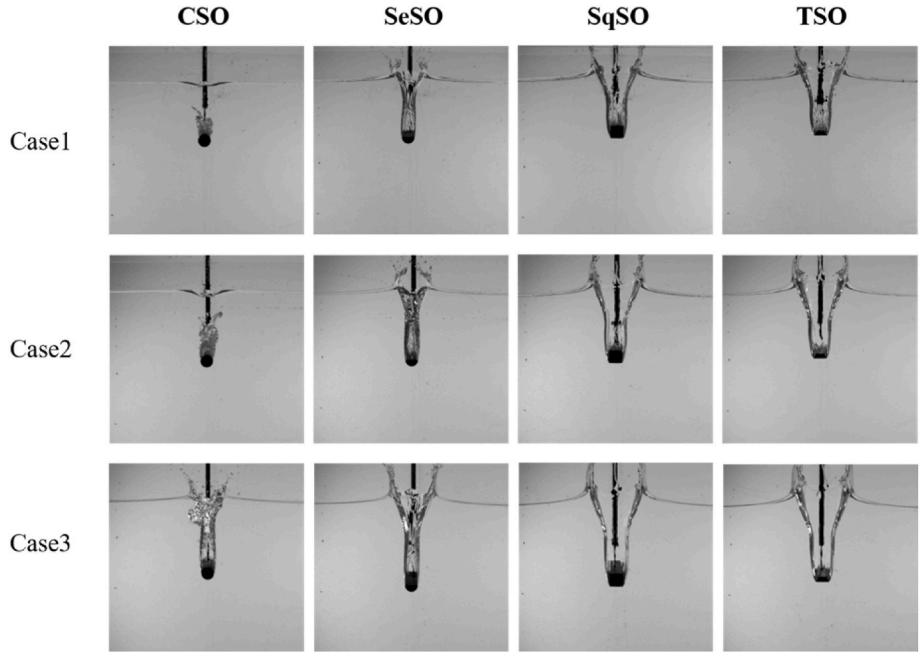

Fig. 4. The image of the water entry cavity formed by four test objects at $t = 0.075$s for the three cases.

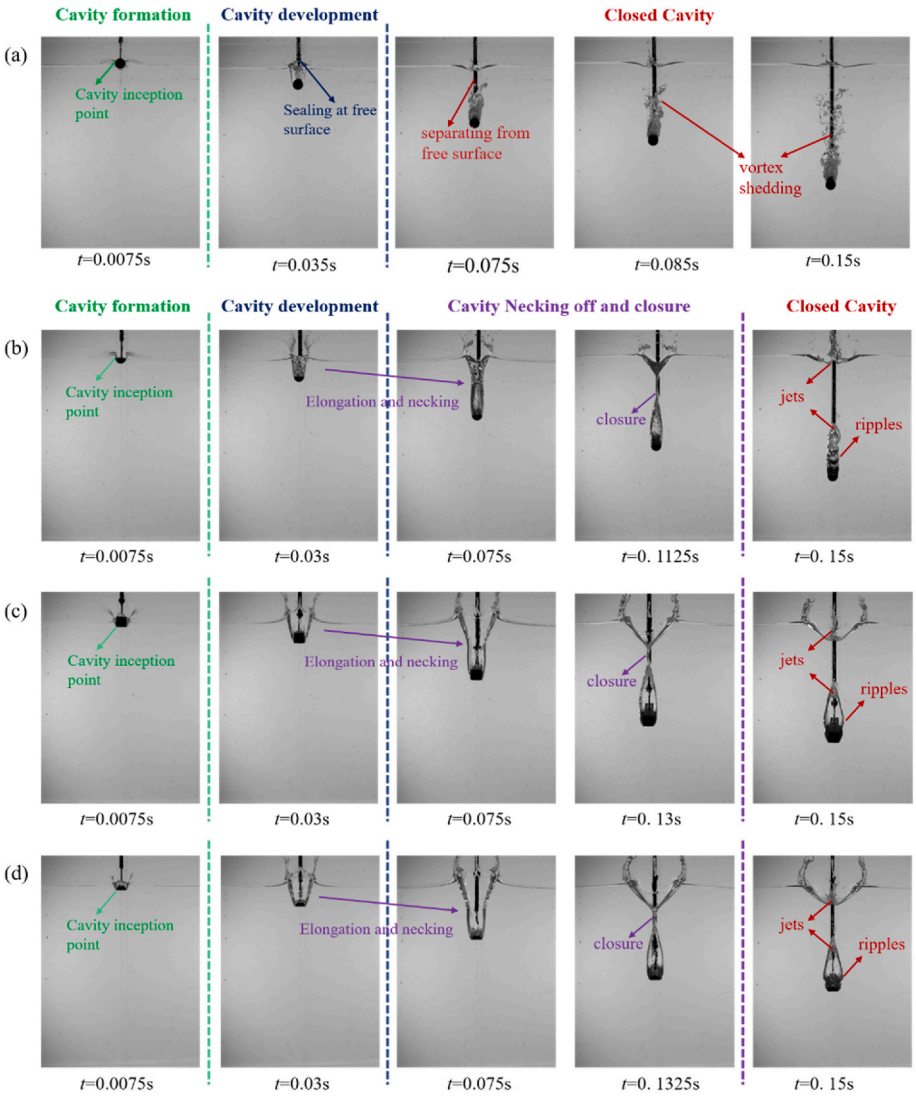

Fig. 5. The image sequences of the water-entry cavity formed by four test objects of Case2.

where $\overline{\mathbf{D}}$ denotes the resolved-scale strain rate tensor. The SGS stress tensor $\boldsymbol{\tau_{SGS}}$ is modelled as:

$$\tau_{SGS} = \frac{2}{3}k_{SGS}\mathbf{I} - 2\nu_{SGS}\left(\overline{\mathbf{D}} - \frac{1}{3}tr(\overline{\mathbf{D}})\mathbf{I}\right) \tag{14}$$

The SGS heat flux are simply modelled as:

$$Q_{SGS} = \frac{\overline{\rho}\nu_{SGS}}{\mathrm{Pr}_{SGS}}\nabla\widetilde{T} \tag{15}$$

where Pr_{SGS} is the SGS Prandtl number, taken the value 1.0 in internal computational domain and 0.85 at walls.

3.3. Simulation setup

The simulation is implemented based on the OpenFOAM®, and the solver used in this paper is CompressibleInterDyMFoam which is appropriate to simulate the compressible two-phase flow problems with moving objects. The Volume of Fluid (VOF) method including an

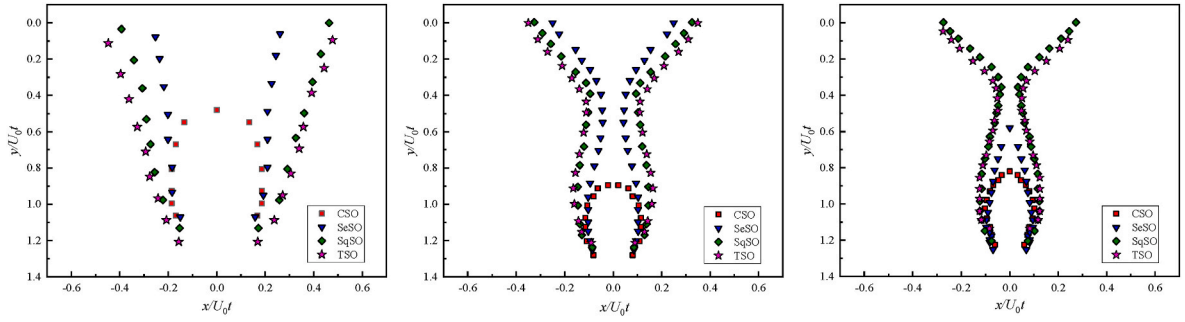

Fig. 6. The cavity profiles at (a)t = 0.05s, (b) t = 0.10s and (c)t = 0.125s, respectively.

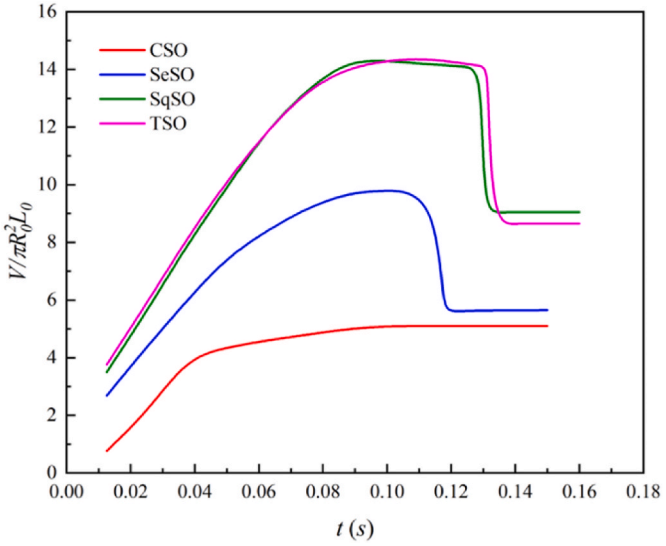

Fig. 7. The dimensionless volume of cavity of the five objects. The cavity volumes V are dimensionless by the volume of circle section object $\pi {R_0}^2 L_s$.

artificial compression term along with the multidimensional universal limiter with explicit solution (MULES) algorithm is used to track the gas-liquid interface. Overset mesh and 6DOF body are used to simulate the entry process of object.

The simulation is simplified to be two-dimensional at y-z plane by setting boundary type of front and back surface face to be empty. The computational domain and boundary are given according to experimental setup as shown in Fig. 3(a), where d is the diameter of the water entry object. The coordinate system is established with the origin on the free surface, the vertical down as the negative direction of y axis, and horizontal right as the positive direction of z axis. Structured mesh is used in this paper and the computational mesh near the water entry object is shown in Fig. 3(b). We also generate a set of coarse mesh and fine mesh and compare the predicted y-coordinate of the center of the cylinder to validate the mesh convergence as shown in Fig. 3(c). Considering both the accuracy of results and the time consumed in the present work, the medium mesh is adopted in our work.

4. Results and discussion

4.1. Cavity evolution

The influences of geometrical shapes on the cavity evolution are investigated in this section. The cavity form of the four objects for the cases listed in Table 1 at typical time are presented in Fig. 4. From the images, it can be seen that the cavity form and seal pattern of CSO is obviously different form SeSO, SqSO and TSO in Case1 and Case2. But for Case3, all the cavities evolution processes are similar in which all cavities experience deep seal. The difference of cavity form between CSO and others in Case1 and Case 2 catches our attention, we will focus on that and emphatically discuss it in this paper.

Taking Case2 as a representative, the cavities developing process is shown in Fig. 5. The corresponding cavity profiles at typical time are displayed in Fig. 6. To further analyze the variation of cavity, the change of cavity volume with time is shown in Fig. 7.

As shown in Fig. 5, for the CSO, in the cavity formation stage the object impacts the water surface, cavity begins to form at the trailing edge of the object. In the cavity development stage, the cavity elongates below the free surface and seals at the free surface at the same time. The cavity is filled with a mixture of water and air, which makes the cavity interface vague. In the closed cavity stage, the cavity separating from free surface (t = 0.075s) at first, then gradually collapses with vortex

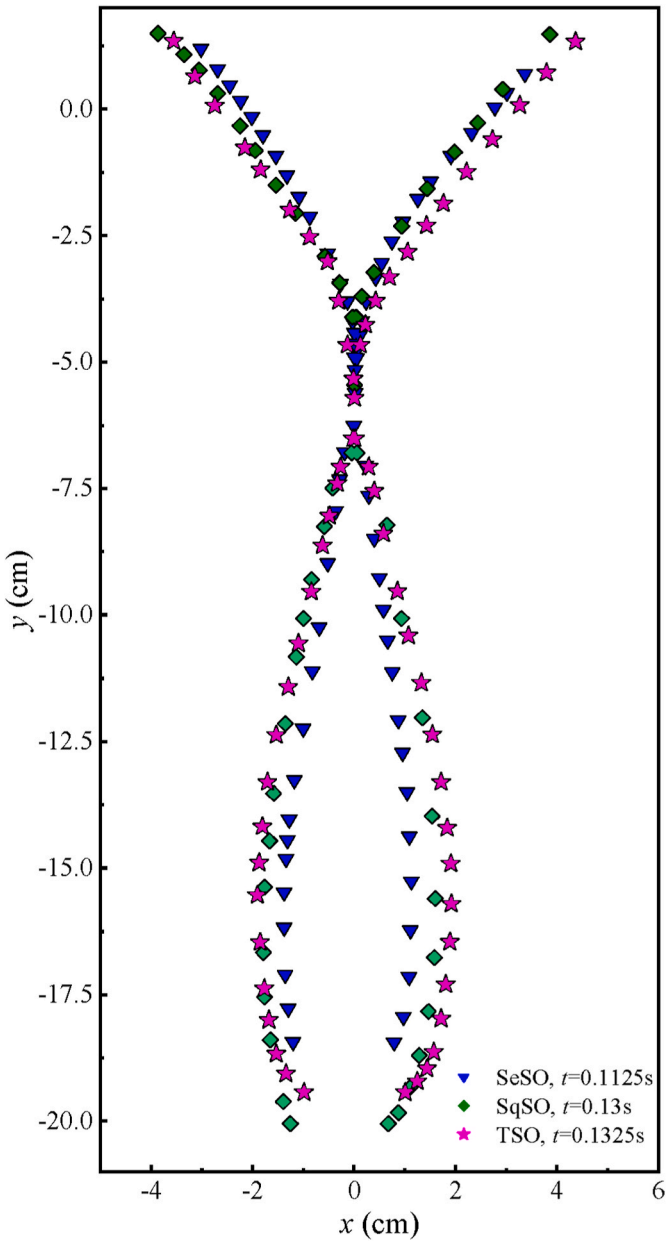

Fig. 8. The cavity at pinch-off time for SeSO, SqSO and TSO.

shedding at the tail (t = 0.085 s–0.15s). The cavity morphology in the experiment can be affected by the water tank wall, to explain the special shape of CSO, we combine the simulation results shown in Fig. 12(a) to illustrate. After impact the free surface, the water film climbs along the circle surface (t = 0.040s–0.01s). Before submerged, the water film begins to separate at the trailing edge to form cavity and have the trend of inward motion. Then, the water film at the two sides get close and finally collide leading to the closure at free surface. After collision, water film jets downwards into cavity to make the content to be the air-water mixture.

For the other three test objects (SeSO, SqSO, TSO), the cavity evolution process is almost the same, containing four stages: cavity formation, cavity development, cavity necking off and closure, and closed cavity. As the objects enter the water, more and more air is entrained, a transparent cavity is evident below the free surface and a splash curtain above. However, there still exists some differences in detail.

In the cavity formation stage (t = 0.0075s), the cavity inception points are different. For the SeSO, the cavity starts to generate only after

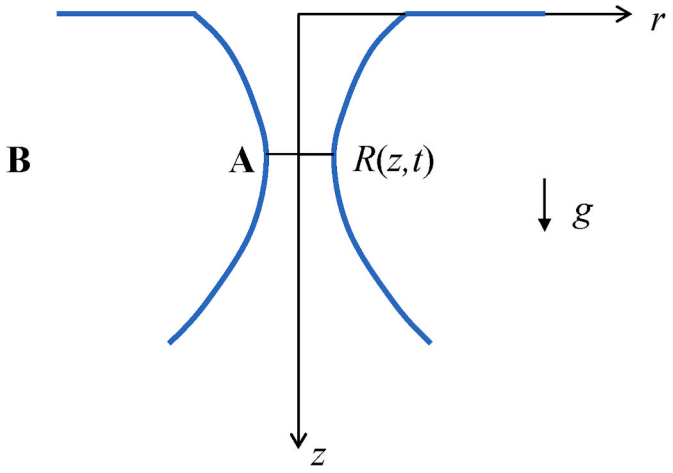

Fig. 9. Conventions used to describe the dynamic of the two-dimension cavity.

the top of the objects is submerged in the water, while for the SqSO and TSO, the cavities form as soon as the objects impact the free surface.

In the cavity development stage, as the objects descend, the cavities gradually elongate and expand in the radial direction. The kinetic energy of fluid from the object supports the radial expansion of cavity. As SqSO and TSO suffer greater resistance during the descending process, the kinetic energy loss is larger, which leads to higher radial velocity of the fluid. Therefore, the cavity radial length in the case of SqSO and TSO is larger than the others at the same depth as shown in Fig. 6(a).

In the cavity necking and closure stage, because of the hydrostatic pressure, the radial velocity of the cavity section gradually decreases to zero at the middle-upper part, and then accelerates in reverse, resulting in the cavity contraction. The necking phenomena appear in the case of SeSO first, followed by SqSO and TSO (Fig. 6(b) and (c)). Necking phenomena effects the rate of volume change, reflected in the decrease of slope at $t = 0.075$–0.115s (shown in Fig. 7). When the contracting boundaries collide and coalesce, cavities will be pinched off named deep seal, which cause the cavity volumes decrease sharply to certain values.

In the closed cavity stage, two jets generate in each of the cases, one goes upwards and the other rushes downwards ($t = 0.15$s). In the meanwhile, ripples appear at the cavity boundary. The cavity volumes stay steady in this stage.

4.2. Pinch-off depth

Pinch-off depth H_p is an important quantity in deep seal. Fig. 8 gives cavity shape at the pinch-off time for Case2. We found that pinch-off depth is very close for the three open cavity cases (SeSO, SqSO and TSO).

In order to explain the influence impact on pinch-off depth, we establish a mathematical model for our two-dimension water entry problem based on the potential theory presented in Fig. 9.

As the impact velocity is relatively low in our study, so we can ignore the effect of aerodynamic force. By analogy with Besant-Rayleigh problem, we assume a purely radial motion $u = \dot{R}$ based on the fluid continuity equation, which leads to

$$\varphi = \dot{R}r,\ R < r < R_\infty = 0, r > R_\infty \tag{16}$$

Following the approach used to solve the Besant–Rayleigh problem, we consider the generalized Bernoulli equation including gravity:

$$\left[\frac{\partial\varphi}{\partial t} + \frac{u^2}{2} + \frac{p}{\rho} - gz\right]_A^B = 0 \tag{17}$$

Selecting point A in the liquid behind the interface and point B at the same height ($z_B = z_A = z$) but far from the cavity, we obtain

Table 2
The parameters value for the evaluation of theoretical pin-off depth.

Parameters	ε	$\sqrt{\alpha}$	η
Value	0.0436	0.05–0.20	18.44–20.05

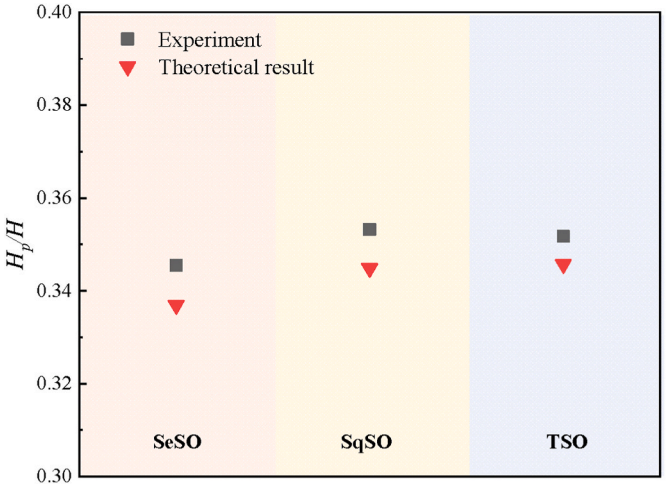

Fig. 10. Comparison of the pinch-off depth between the experimental and theoretical evaluation.

$$\left.\frac{\partial\varphi}{\partial t}\right|_R + \frac{\dot{R}^2}{2} = -gz \tag{18}$$

Then take the time derivative with respect to the potential φ, we get

$$\frac{\partial\varphi}{\partial t} = \ddot{R}r + \dot{R}u \tag{19}$$

Using this expression, we can simplify the momentum equation (19) and get the equation for the cavity:

$$\frac{3}{2}\dot{R}^2 + \ddot{R}R = -gz \tag{20}$$

Equation (21) has the same form with Duclaux et al. (2007), the time evolution of the radius of the air cavity can be written in a dimensionless form

$$\overline{R}^2 = 1 + 2\sqrt{\alpha}\eta(1-\overline{z}) - \varepsilon\eta^3\overline{z}(1-\overline{z})^2$$

Here, $\overline{R} = R/R_0$, $\eta = H/R_0$, $\overline{z} = z/H$, $\varepsilon = 1/Fr = (gR_0)/U^2$, H is the cavity depth and z is the depth. The initial conditions $R(t=0) = R_0$ and $\dot{R}(t=0) = \sqrt{\alpha}U$ are applied, and α is a constant smaller than 1. At the pinch-off position, $R = 0$; then the solutions of $\overline{z}$ can be expressed as:

$$\overline{z}_{min} = \frac{2}{3} - \frac{1}{3}\sqrt{1 - 6\frac{\sqrt{\alpha}}{\varepsilon\eta^2}} \tag{21}$$

Here $\overline{z}_{min}$ is the location of the minimum (pinch-off position) radial extent of the cavity.

We extract the dimensionless parameters (see Table 2) to evaluate the theoretical pinch-off depth and compare it with experimental one as shown in Fig. 10. According to the theoretical analysis, it indicates that the H_p/H keeps almost unchanged in the condition of Case2.

Even though the different objects have different $\sqrt{\alpha}$, but it is much smaller than the $\varepsilon\eta^2$, so the dimensionless pinch-off depth is close to 1/3.

4.3. Flow fields based on simulation results

In order to explore the influence of geometrical shapes on water

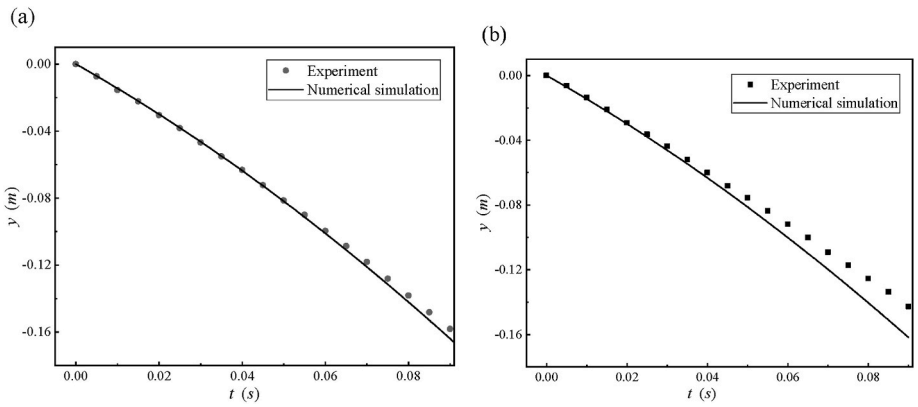

Fig. 11. The of variation vertical depths with time of simulation and experimental results (a. CSO b. TSO).

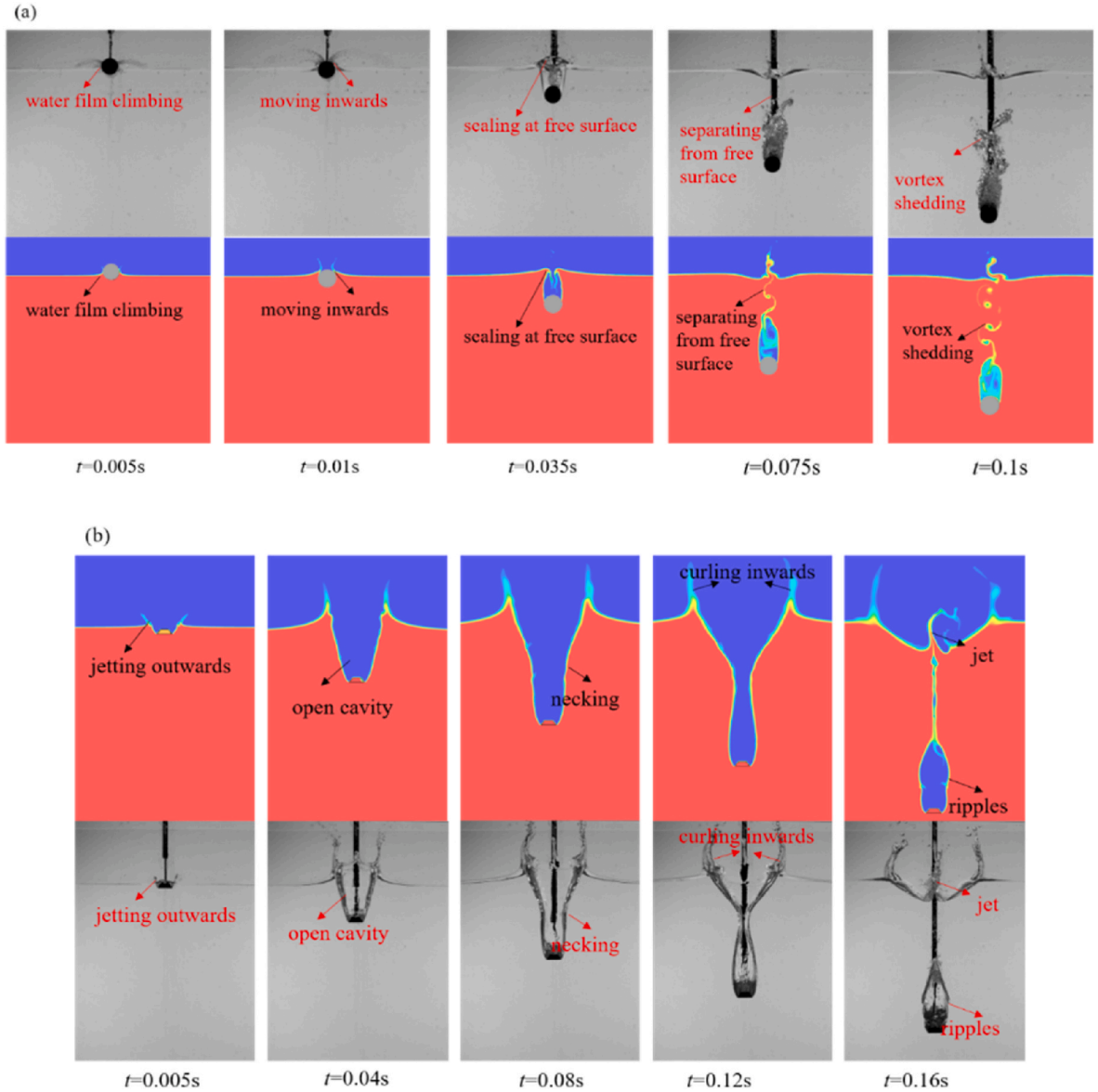

Fig. 12. Comparison of cavity evolution between the experimental and the numerical results (a. CSO b. TSO). The initial time is taken as the moment the bottom of the solid arrive the free surface.

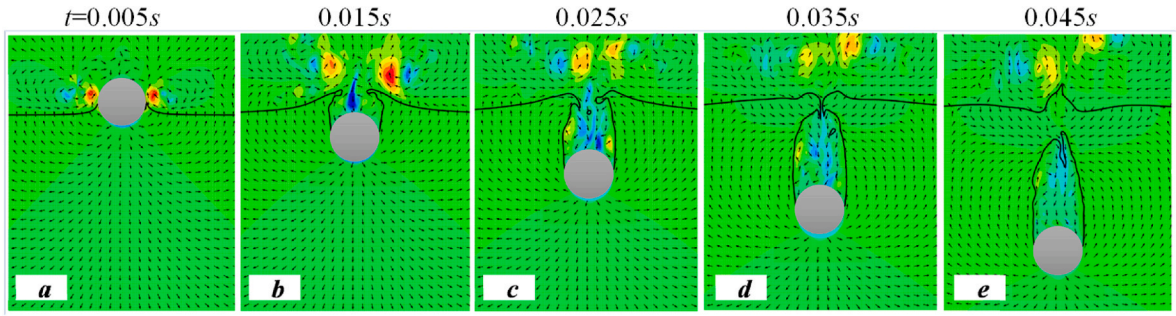

Fig. 13. Vertical velocity V and vector field caused by CSO.

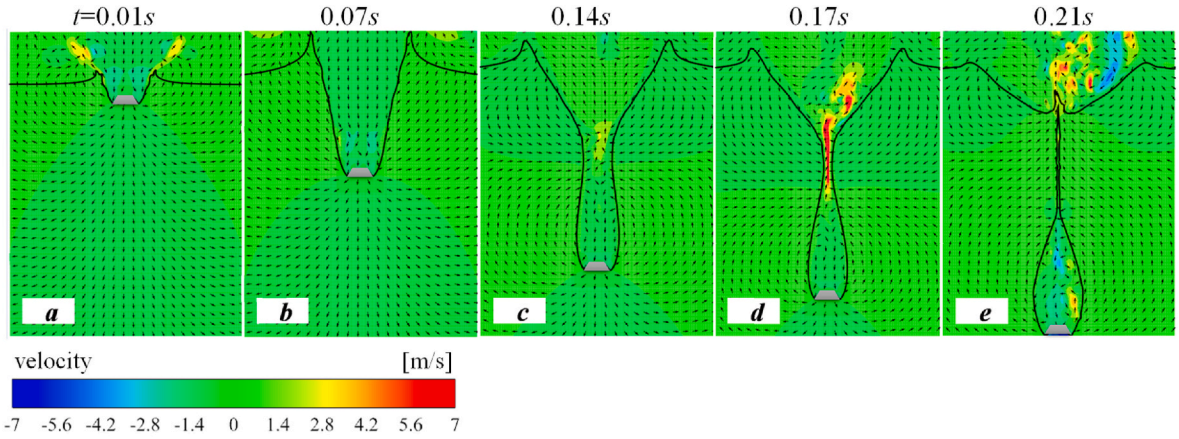

Fig. 14. Vertical velocity V and vector field caused by TSO. The vector represents direction only, not magnitude.

entry flow fields in Case2, the CSO and TSO are chosen as the typical cases to conduct simulations. The numerical methods have been introduced in section 3.

4.3.1. Validation

In order to validate the numerical method, the variation of vertical depths with time and instantaneous cavity evolution between numerical and experimental results during water entry process are compared in Fig. 11 and Fig. 12, respectively. From Fig. 11, the experimental data are slightly smaller than the numerical data due to the frictional resistance of the launching system. However, the small discrepancy between them is considered acceptable. Fig. 12 shows that the cavity evolution captured by the numerical method is basically in agreement with the experiment.

4.3.2. Comparison of cavity flow fields

To explain the relationship between the velocity and water entry phenomenon. We first extract the vertical velocity V for two objects at typical time are presented in Fig. 13 and Fig. 14. In the initial stage, it can be seen that the splash sprays at a relative high speed after the objects impact the free surface (as shown in Figs. 13(a) and 14(a)). In the development stage, for the CSO, the water films on the two sides move inwards and get close to each other, which makes the cavity entrance narrow, and the air flow enters the cavity at a relative high speed (Fig. 13(b)). Then with the collision of the two water films, the air flow vortices above the free surface moves closer (Fig. 13(c)&d). After the cavity seal, the coalesced water film moves upwards, and the velocity inside cavity tends to decrease (Fig. 13(e)).

As for water entry of TSO, in the development stage, the cavity entrance is wide, and the air flow can enter into the cavity smoothly which leads to a uniform velocity field (Fig. 14(b)). When it comes to necking stage, the contraction of cavity boundary extrudes the air resulting in the upward acceleration of air flow (Fig. 14(c) and (d)). After the deep seal of the cavity, the jets caused by pinch off began to move rapidly in the opposite direction (Fig. 14(e)).

The vertical velocity V is highly relevant to the splashes and air flow into the cavity. In addition, the radial velocity W can reflect the cavity evolution to some extent. According to the equation (20) which models the cavity evolution and its initial condition, the cavity development is related to the ratio of radial velocity $\sqrt{\alpha}$. From Aristoff and Bush (2009), $\sqrt{\alpha}$ is relevant to the cone angle θ_c:

$$\tan\left(\theta_c - \frac{\pi}{2}\right) = \frac{U_0 dt}{\dot{R}(t=0)dt} = \frac{1}{\sqrt{\alpha}} \tag{22}$$

The difference in cone angle θ_c between CSO and TSO is related to contact surface between object and fluid as shown in Fig. 15. Because of the curved surface of CSO, the fluid flows along the surface at first and then separates at the cavity inception point near the equator, after that, it moves along the direction closed to the tangent line. Thus, θ_c is more closed to 180° and $\sqrt{\alpha}$ is smaller. As for TSO, the flat surface extrudes the fluid below, and the fluid separates at the cavity inception point with higher horizontal velocity at a cone angle θ_c smaller than that of CSO. Therefore, the cavity expansion velocity of TSO is higher than CSO leading to the difference in cavity evolution.

4.4. The evolution of vortex structures

During the process of water entry, multiscale vortices will be produced by large velocity and pressure gradient, which shows great unsteady characteristics. To study the evolution of vortex structures caused by different objects, the vorticity distribution at the typical time is displayed in Fig. 16 and Fig. 17.

As for the CSO (as shown in Fig. 16), above the free surface, a pair of large-scale vortices form due to the existence of splashes. Below the free

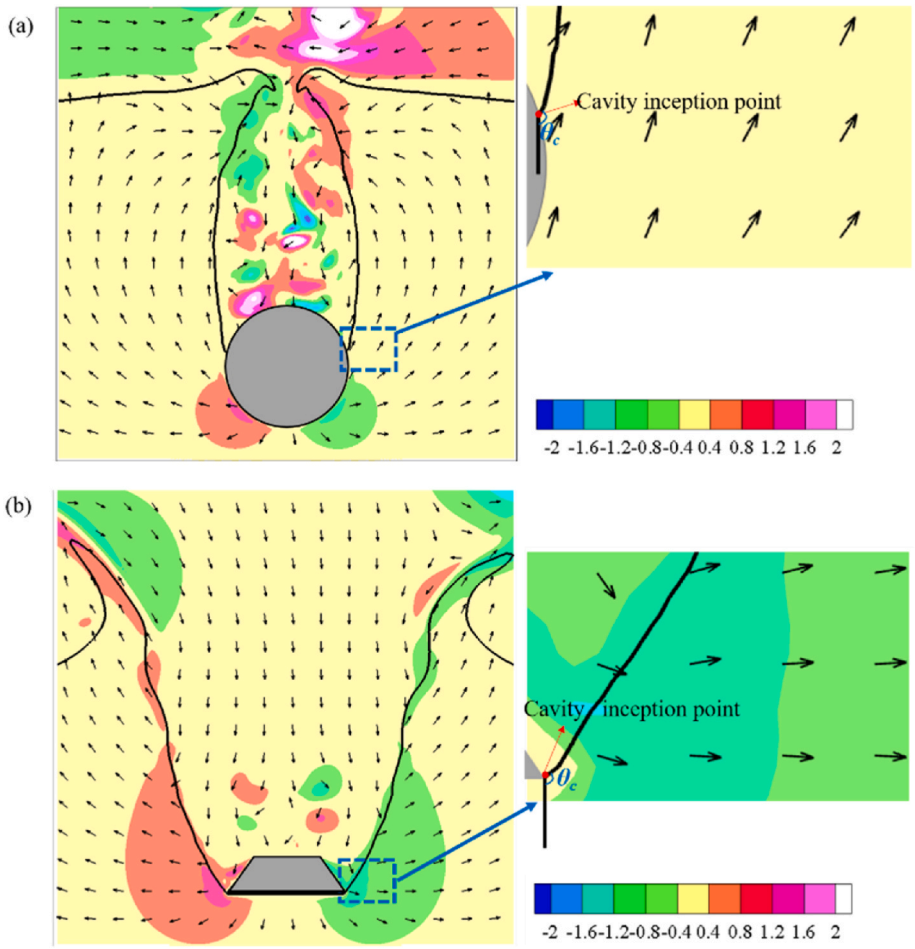

Fig. 15. The radial velocity W in the cavity development stage. (a) CSO (b) TSO. The isolines with a volume fraction of 0.5 of water was extracted to represent the cavity profile. The vector represents direction only, not magnitude. The enlarged image shows the flow field and cone angle near the cavity inception point.

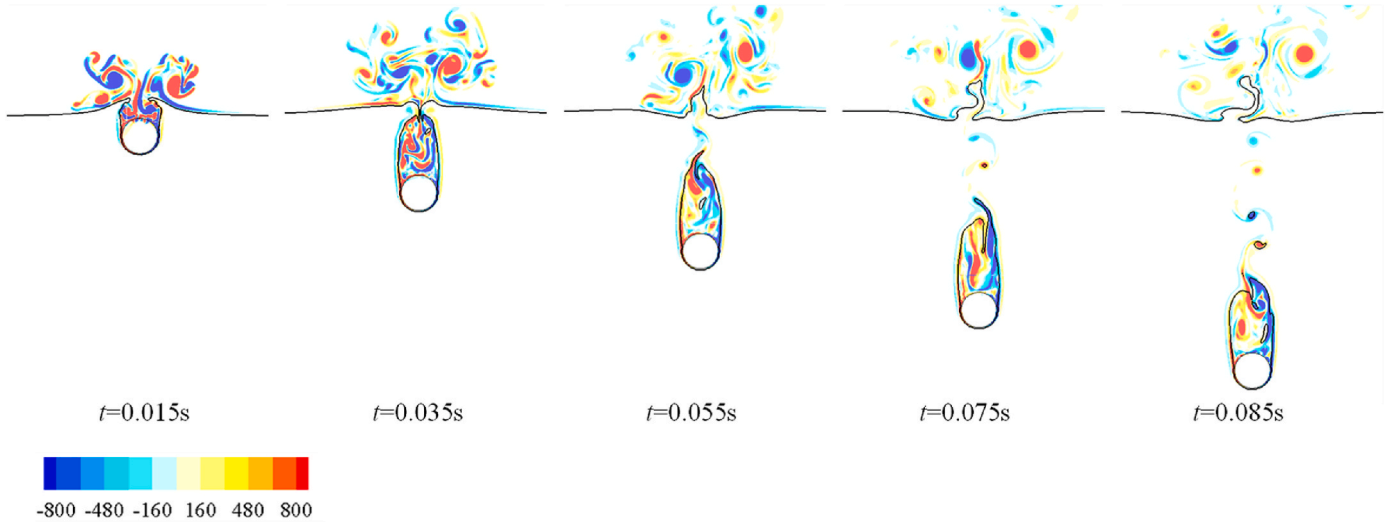

Fig. 16. The vortex evolution of CSO.

surface, before the cavity seal (at $t = 0.015$s), air flow continually rushes into the cavity and interacts with the water, which produces more small-scale vortices. After the cavity seal, the cavity separates from the free surface at first, then the vortices alternately shed at the tail of cavity. With the increase of the depth, the pressure difference inside and outside the cavity becomes larger, and it promotes the gas leakage from the cavity to form vortices.

In terms of the TSO (as shown in Fig. 17), at $t = 0.075$s, the wide cavity entrance makes the airflow to entry smoothly and the vortices are suppressed by the cavity interface. When it comes to cavity necking stage ($t = 0.135$s), the airflow moves upwards rapidly leading to the increase of vorticity. In the closed cavity stage, the vortices are produced

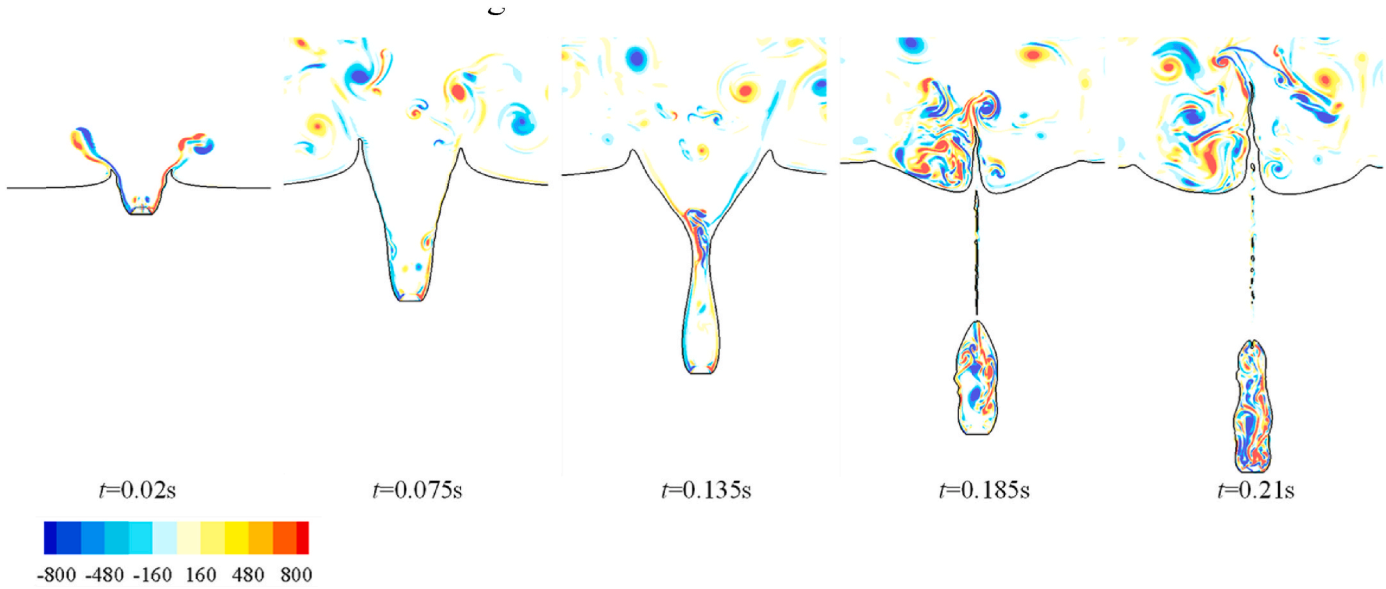

Fig. 17. The vortex evolution of TSO.

by the pinch-off jets ($t = 0.185$s). It is worth mentioning that, unlike the case of CSO, the closed cavity is squashed by hydrostatic pressure and gets distorted at once ($t = 0.21$s) without alternating vortex shedding immediately.

5. Conclusion

In this study, the water entry problem of horizontal objects with different geometrical shapes of was investigated experimentally and numerically. The cavity evolutions were captured by high-speed photography. A compressible two-phase solver on OpenFOAM® platform is adopted to simulate the water entry of two typical objects through LES turbulence model and overset mesh technology. A reasonable agreement between the numerical and experimental results indicates the effective capability of the employed numerical method to capture the flow details during the water entry. The results show that the geometrical shape has great effect on the cavity size and evolution. However, for the open cavity cases (SeSO, SqSO and TSO), the pinch-off depth is slightly affected by the geometrical shape. Furthermore, the two typical cases CSO and TSO are analyzed to explain the effect of geometrical shape on the cavity dynamics. The cavity radial development is relevant to differences of cone angle θ_c which is dependent on the contact surface of fluid and solid. After impact, the fluid near the cavity inception points of TSO has the tend to move more horizontally because of the flat bottom surface. For CSO, the fluid around the CSO moves along the curved surface at first and then separates at cavity inception points near the equator with the trend of moving vertically. It caused the higher expansion velocity in radial for TSO which leads to the difference of cavity evolution between CSO and TSO. The vortex structures are closely related to the cavity evolution, so it results in apparent differences in the vortex structures of these two objects.

CRediT authorship contribution statement

Yan Du: Conceptualization, Methodology, Software, Investigation, Validation, Formal analysis, Writing – original draft. **Zhiying Wang:** Conceptualization, Methodology, Investigation, Writing – review & editing. **Yiwei Wang:** Methodology, Review, Funding acquisition, Supervision. **Jingzhu Wang:** Methodology, Investigation, Review. **Rundi Qiu:** Methodology, Formal analysis. **Chenguang Huang:** Methodology, Review.

Declaration of competing interest

The authors declare that they have no known competing financial interests or personal relationships that could have appeared to influence the work reported in this paper.

Acknowledgement

This work was supported by the National Natural Science Foundation of China (12122214 and 11902323) and the Youth Innovation Promotion Association CAS (Y201906 and 2022019).

References

Abrate, S., 2013. Hull slamming. Appl. Mech. Rev. 64 (6), 060803.
Aristoff, J.M., Bush, J.W.M., 2009. Water entry of small hydrophobic spheres. J. Fluid Mech. 619, 45–78.
Aristoff, J.M., Truscott, T.T., Techet, A.H., Bush, J.W.M., 2010. The water entry of decelerating spheres. Phys. Fluids 22 (3), 032102.
Bergmann, R., Van Der Meer, D., Gekle, S., Van Der Bos, A., Lohse, D., 2009. Controlled impact of a disk on a water surface: cavity dynamics. J. Fluid Mech. 633, 381–409.
Bodily, K.G., Carlson, S.J., Truscott, T.T., 2014. The water entry of slender axisymmetric bodies. Phys. Fluids 26 (7), 072108.
Chen, T., Huang, W., Zhang, W., Qi, Y., Guo, Z., 2019. Experimental investigation on trajectory stability of high-speed water entry projectiles. Ocean. Eng. 175, 16–24.
Duclaux, V., Caille, F., Duez, C., Ybert, C., Bocquet, L., Clanet, C., 2007. Dynamics of transient cavities. J. Fluid Mech. 591, 1–19.
Duez, C., Ybert, C., Clanet, C., Bocquet, L., 2007. Making a splash with water repellency. Nat. Phys. 3 (3), 180–183.
Enriquez, O.R., Peters, I.R., Gekle, S., Schmidt, L.E., Lohse, D., van der Meer, D., 2012. Collapse and pinch-off of a non-axisymmetric impact-created air cavity in water. J. Fluid Mech. 701 (32), 40–58.
Gekle, S., van der Bos, A., Bergmann, R., van der Meer, D., Lohse, D., 2008. Noncontinuous Froude number scaling for the closure depth of a cylindrical cavity. Phys. Rev. Lett. 100 (8), 084502.
Glasheen, J.W., Mcmahon, T.A., 1996. Vertical water entry of disks at low froude numbers. Phys. Fluids 8, 2078–2083.
Korkmaz, F.C., Guzel, B., 2017. Water entry of cylinders and spheres under hydrophobic effects; Case for advancing deadrise angles. Ocean. Eng. 129, 240–252.
Li, D.Q., Zhao, X., Kong, D.C., Shentu, J.Z., Wang, G.Y., 2020. Numerical investigation of the water entry of a hydrophobic sphere with spin. Int. J. Multiphas. Flow 126, 103234.
Mansoor, M.M., Marston, J.O., Vakarelski, I.U., Thoroddsen, S.T., 2014. Water entry without surface seal: extended cavity formation. J. Fluid Mech. 743, 295–326.
May, A., 1953. Vertical entry of missiles into water. J. Appl. Phys. 23, 1362–1372.
May, A., 1975. Water Entry and the Cavity-Running Behavior of Missiles. Nasa Sti/recon Technical Report N.
May, A., Woodhull, J.C., 1950. The virtual mass of a sphere entering water vertically. J. Appl. Phys. 21 (12), 1285–1289.

Seddon, C.M., Moatamedi, M., 2006. Review of water entry with applications to aerospace structures. Int. J. Impact Eng. 32 (7), 1045–1067.
Shi, Y., Wang, G.H., Pan, G., 2019. Experimental study on cavity dynamics of projectile water entry with different physical parameters. Phys. Fluids 31 (6), 067103.
Shi, Y., Hua, Y., Pan, G., 2020. Experimental study on the trajectory of projectile water entry with asymmetric nose shape. Phys. Fluids 32 (12), 122119.
Song, Z.J., Duan, W.Y., Xu, G.D., Zhao, B.B., 2020. Experimental and numerical study of the water entry of projectiles at high oblique entry speed. Ocean. Eng. 211, 107574.
Sruthi, C., Sriram, V., 2017. Wave impact load on jacket structure in intermediate water depth. Ocean. Eng. 140, 183–194.
Sun, T.Z., Wang, H., Zou, L., Zong, Z., Li, H.T., 2019. Experimental study on the cavity dynamics of oblique impact of sphere on a viscous liquid floating on water. Ocean. Eng. 194, 106597.
Sun, T.Z., Wang, H., Shi, C.B., Zong, Z., Zhang, G.Y., 2021. Experimental study of the effects of a viscous liquid layer on the cavity dynamics of vertical entry by a sphere into water at low Froude number. Phys. Fluids 33 (1), 013308.
Vincent, L., Xiao, T., Yohann, D., Jung, S., Kanso, E., 2018. Dynamics of water entry. J. Fluid Mech. 846, 508–535.
Von Karman, T., 1929. The impact on seaplane floats during landing. NACA Tech. Rep. 321.
Wang, X., Shi, Y., Pan, G., Chen, X., Zhao, H.R., 2021. Numerical research on the high-speed water entry trajectories of AUVs with asymmetric nose shapes. Ocean. Eng. 234 (37), 109274.
Wei, Z., Hu, C., 2014. An experimental study on water entry of horizontal cylinders. J. Mar. Sci. Technol. 19 (3), 338–350.
Yan, G.X., Pan, G., Shi, Y., 2019. Experimental study on water entry of cylindrical projectiles with different nose shapes. Mod. Phys. Lett. B 33 (9), 1950107.
Zhao, R., Faltinsen, O., 1993. Water entry of two-dimensional bodies. J. Fluid Mech. 246, 593–612.